

**Influence of electrode contact arrangements on
Polarisation-Electric field measurements of ferroelectric
ceramics: A case study of BaTiO₃**

CARROLL, Erin L., KILLEEN, James H., FETEIRA, Antonio
<<http://orcid.org/0000-0001-8151-7009>>, DEAN, Julian S. and SINCLAIR,
Derek C.

Available from Sheffield Hallam University Research Archive (SHURA) at:

<https://shura.shu.ac.uk/34218/>

This document is the author deposited version. You are advised to consult the publisher's version if you wish to cite from it.

Published version

CARROLL, Erin L., KILLEEN, James H., FETEIRA, Antonio, DEAN, Julian S. and SINCLAIR, Derek C. (2024). Influence of electrode contact arrangements on Polarisation-Electric field measurements of ferroelectric ceramics: A case study of BaTiO₃. *Journal of Materiomics*: 100939. [Article]

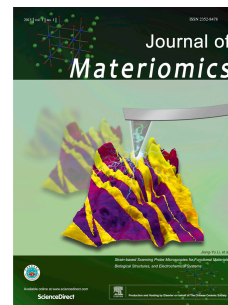
Copyright and re-use policy

See <http://shura.shu.ac.uk/information.html>

Journal Pre-proof

Influence of electrode contact arrangements on Polarisation-Electric field measurements of ferroelectric ceramics: A case study of BaTiO₃

Erin L. Carroll, James H. Killeen, Antonio Feteira, Julian S. Dean, Derek C. Sinclair



PII: S2352-8478(24)00178-3

DOI: <https://doi.org/10.1016/j.jmat.2024.100939>

Reference: JMAT 100939

To appear in: *Journal of Materiomics*

Received Date: 1 May 2024

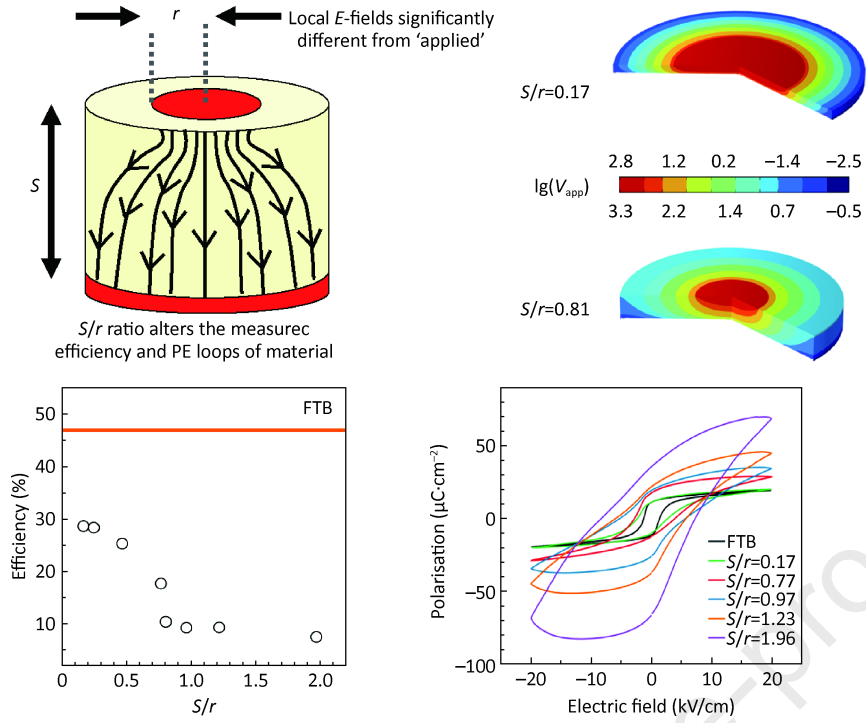
Revised Date: 3 August 2024

Accepted Date: 13 August 2024

Please cite this article as: Carroll EL, Killeen JH, Feteira A, Dean JS, Sinclair DC, Influence of electrode contact arrangements on Polarisation-Electric field measurements of ferroelectric ceramics: A case study of BaTiO₃, *Journal of Materiomics*, <https://doi.org/10.1016/j.jmat.2024.100939>.

This is a PDF file of an article that has undergone enhancements after acceptance, such as the addition of a cover page and metadata, and formatting for readability, but it is not yet the definitive version of record. This version will undergo additional copyediting, typesetting and review before it is published in its final form, but we are providing this version to give early visibility of the article. Please note that, during the production process, errors may be discovered which could affect the content, and all legal disclaimers that apply to the journal pertain.

© 2024 Published by Elsevier B.V. on behalf of The Chinese Ceramic Society.



Influence of electrode contact arrangements on Polarisation-Electric field measurements of ferroelectric ceramics: A case study of BaTiO₃

Erin L Carroll^a, James H. Killeen^a, Antonio Feteira^b, Julian S Dean^a and Derek C Sinclair^{a*}

^a Department of Materials Science and Engineering, Sir Robert Hadfield Building, University of Sheffield, Mappin Street, Sheffield S1 3JD, United Kingdom

^b Materials and Engineering Research Institute, Sheffield Hallam University, Sheffield S1 1WB, United Kingdom

* Corresponding Author

Abstract: A range of partial top full bottom electrodes are used to explore the use of bi-polar Polarisation-Electric field (P - E) measurements to quantify recoverable energy (W_{rec}), energy loss (W_{loss}) and the efficiency (η) of ferroelectric BaTiO₃ ceramics. The values obtained are dependent on the ratio of sample thickness (S) and top contact radius (r). With increasing S/r from 0.17 to 1.96 the P - E responses become increasingly distorted and broader. Measurements show W_{rec} increases by a factor of ~ 1.4 but W_{loss} increases by a factor of ~ 7 with η decreasing from $\sim 29\%$ to 8% . Finite element modelling was used to simulate the experimental set-up of the sample/electrode arrangements using the Jiles-Atherton model to replicate the ferroelectric behaviour of BaTiO₃. These models demonstrate the experimentally applied electric field using a simple geometric correction for sample thickness is an underestimation of the actual field experienced by the material under the top contact at high S/r values. We stress the importance of reporting the contact sizes and thicknesses of samples when using P - E measurements to assess W_{rec} , W_{loss} and η in non-linear dielectric materials. This will allow a fairer comparison of performances between various types of materials being considered for high-energy-density ceramic capacitors.

1. Introduction

The demonstration of Polarisation-Electric field (P - E) hysteresis loops has been used since 1930 to identify ferroelectric materials and establish parameters such as remanent and saturated polarisation, P_r and P_s , respectively along with the coercive field, E_c , Fig. 1. In many cases, for high permittivity (non-conducting) ferroelectrics, the polarisation P at a given time is very nearly equal to the electric displacement, D ; however, a small correction is needed for the dielectric displacement to give accurate results for low permittivity dielectrics *via* Equation 1,

$$D(t) = \varepsilon_0 E(t) + P(t)$$

Equation (1)

where ϵ_0 is the permittivity of free space, E is the electric field and t is the time. This leads to D and P being interchangeable, and as such many ferroelectricians refer to their measurements as P - E loops. This holds true if the polarisation of the material is given by

$$P = \frac{Q}{2A} = \frac{\int Idt}{2A} \quad \text{Equation (2)}$$

where Q is the total switched charge over the area A of the electrodes on the sample (assuming the two contacts are of identical area), related to the total integrated current I , which is generated by the ferroelectric domain switching. However, this assumption and measurement pose significant issues for electrically leaky materials and can lead to ambiguity, either as an erroneous diagnosis of ferroelectricity in a non-ferroelectric material or inconclusive evidence for ferroelectricity. If the material has significant conduction (*i.e.* a leaky-dielectric) then the measured current, and as such, charge requires an additional term that is related to the electrical conductivity, σ , of the material and the electric field given by

$$Q = 2PA + \sigma EAt \quad \text{Equation (3)}$$

The assumption that D and P are directly interchangeable no longer holds. Therefore, if the conductivity of the material is high or becomes high during the measurements (for example under high electric fields), the polarisation due to domain switching will be swamped in a signal that now includes contributions from the electrical conductivity (and the dielectric displacement) with ‘cigar’-like loops produced. This is well documented in standard textbooks [1] and, more famously in the article ‘Ferroelectrics go bananas’ [2]. As much of the current literature ignores this when presenting their data, for present (illustrative) purposes we shall also refer to our data as P - E loops.

With the recent interest in the development of high energy density and high-efficiency dielectric capacitors for power electronics [3–6], P - E loop measurements are increasingly being used to quantify energy storage density, W_{rec} , and energy loss density, W_{loss} , to provide an overall efficiency of the capacitor, η , where $\eta = W_{\text{rec}}/(W_{\text{rec}} + W_{\text{loss}})$, Fig. 1 [7–10]. Additionally, these materials need to operate at higher temperatures (*e.g.* 200–300 °C) and electric fields (*e.g.* > 200 kV/cm), thus requiring high breakdown strength. P - E testing therefore requires high electric fields to be generated and arcing effects between the electrodes to be minimised. Based on a top-bottom electrode arrangement, users typically measure thin samples (recall E = applied voltage/distance of electrode separation) and/or electrode configurations that are not full top-bottom (FTB) but partial (micro) top-full bottom (mTFB) or symmetrical micro-top, micro-bottom in attempts to overcome these issues.

There are several methods based on various measured quantities (in brackets) to establish electric-field induced polarisation, for example, Sawyer-Tower (charge), current step (voltage) and virtual ground (current) [11]. In all cases, the principle is based on quantifying the switched charge, Q , against an applied voltage, V_{app} , at a certain frequency. Users are required to input the area, A , of the electrodes, usually in units of cm^2 , to convert Q (C) into P (usually plotted as $\mu\text{C}/\text{cm}^2$) along with the distance of electrode separation, S (usually in units of cm or m) to convert V_{app} (V) into E (usually plotted as kV/cm or MV/m). For FTB electrodes conversion of Q to P and V_{app} to E is trivial as A and S are easily identified and E across the material (assuming its ideal and electrically homogeneous and isotropic) is uniform. Challenges arise when the two electrodes are of different size and therefore area. What should the user input for the radius of the electrode to calculate A : the reduced radius of the top electrode, an average of the two electrodes or the radius of the full bottom electrode? Furthermore, E across any ideal material now becomes non-uniform. These issues influence the values obtained for W_{rec} , W_{loss} and η . This has been exemplified by Zhang *et al.* [12] who measured the same NaNbO_3 -based material under FTB and mTFB electrode arrangements using the same instrument but obtained different P - E loop responses. This resulted in W_{rec} increasing by a factor of ~ 2 and an increase in η from 33 (FTB configuration) to 47% (mTFB configuration) compared to a FTB arrangement. This highlights the need to consider metrology when testing and characterising dielectric materials for high energy density and high-efficiency ceramic capacitor applications using P - E measurements.

The simplest scenario in any electrical measurement uses fully terminated top and bottom surface (FTB) electrodes on an ideal linear dielectric that obeys Ohm's law at low electric fields, as shown in Fig. 2a. This gives rise to a uniform flow of current between the contacts based on a material with uniform permittivity, ϵ , and conductivity, σ . The measured resistance R (Ω) can be converted to σ (usually S/cm) using Equation 4

$$R = \frac{1}{\sigma} \frac{S}{A} \quad \text{Equation (4)}$$

where the ratio S/A is known as the geometric correction factor based on the separation (S) and the area of the electrode. The electric field can be written as

$$E = \frac{V_{app}}{S} = \frac{1}{\sigma} \frac{I_{app}}{A} \quad \text{Equation (5)}$$

where V_{app} and I_{app} are the applied voltage and drawn current on or through the electrode, respectively.

Low-field measurements on ceramics using Impedance Spectroscopy are typically made with fully contacted samples; however, to reach the higher fields required to measure some of the best-performing energy density materials using P-E measurements requires > 200 kV/cm. This is where micro-contacts based on mTFB and thin samples of various dimensions are employed, Fig. 2b–2f and various scenarios associated with charge storage and current flow occur.

When a micro-contact is used in electrical measurements it is no longer a system with simple linear flow. As the top contact is smaller than the bottom, the current can spread out to reduce the resistance by increasing the area over which it is acting, as shown in Fig. 2b.

If a circular contact is assumed to be on a large sheet of homogenous isotropic material with space to spread out unimpeded as depicted in Fig. 2c the spreading resistance can be calculated as

$$R = \frac{1}{\sigma} \frac{1}{4r_{mc}}$$

Equation (6)

where r_{mc} is the micro-contact radius. Fleig and Maier [13] have shown that the region of high current density (75% of the total current density), which dominates the electrical response, is within a hemispherical volume that extends a distance of approximately $4r_{mc}$ from the surface of the contact. Hence, the geometric factor (Eqn. 4) is not associated with the thickness of the sample but inversely proportional to four times the micro-contact radius. This is shown schematically in Fig. 2c as the dark blue region under the micro-contact. In many experimental configurations, however, this ideal scenario of unimpeded spreading resistance is not present and various forms of geometrical confinement occur that can give rise to current confinement and/or interference effects [14], Fig. 2d–2f along with other effects such as hinderance arising from voids and cracks [15].

If the sample is relatively thick but the micro-contact is large with respect to the sample surface area, the spreading current is close to the external surfaces, as in Fig. 2d. The current can no longer spread out freely but is confined and therefore increases the measured resistance. If the micro-contact is small and the sample is thin, confinement is not an issue; however, the high current density envelope under the micro-contact now begins to overlap with the lower electrical contact, leading to current interference and a decrease in the measured resistance, Fig. 2e. Interference and confinement effects can occur in the same system as shown in Fig. 2f. In some scenarios, they are beneficial and act to counterbalance each other to produce near-accurate R values for σ . However, this requires precise geometries and in many cases, interference and/or confinement effects introduce significant errors when using mTFB electrode arrangements [14] to establish the σ of a

material. The ratio of the sample thickness against the micro-contact radius, S/r , provides a useful metric to indicate the level electrical interference that may be present.

Current density, J , and electric field are linked through the conductivity of the material (assuming Ohmic behaviour, *i.e.* $J = \sigma E$) and therefore the spreading of the current leads to a spreading and localisation of the electric field. The electric field a material experiences under the electrical contact can therefore be significantly different to that assumed by Equation 5. To study the significance of this we combine an experimental and modelling approach on the classic ferroelectric material BaTiO₃ to investigate how S/r can affect P - E measurements performed under high electric fields and therefore influence the extracted values of W_{rec} and W_{loss} and consequently η .

2. Experimental section

Undoped BaTiO₃ ceramics were fabricated using a commercially available BaTiO₃ powder with an average particle size of 200 nm. Green pellets were pressed using a uniaxial press followed by isostatic cold pressing and sintered in air at 1350 °C for 5 hours. The resulting ceramics were polished using SiC abrasive paper with isopropanol as a lubricant to ensure the desired thickness of the ceramics. To generate micro-contacts (top) with r between \sim 0.50 mm and 2.00 mm, laser-cut stencils of different radii were used. The top electrode (one per sample) was formed using Au paste, which was heated at 200 °C for 5 minutes. The full bottom electrode was also applied using Au paste and ceramics with mTFB electrodes were heated to 850 °C for 2 hours to harden the Au electrodes. The final diameter of the samples was \sim 7.7 mm to 7.8 mm and a range of thickness (S between \sim 0.3 mm and 1.0 mm) and contact sizes used to produce S/r ratios between 0.17 and 1.96, see supporting information Table SI1.

P - E loops of mTFB electrode ceramics heated to 30 °C and measured at 1 Hz were obtained using a TF Analyzer 2000E with an FE-Module and aixPlover Software. 30 °C was selected to avoid the orthorhombic to tetragonal crystallographic transition in undoped BaTiO₃ at \sim 22 °C. Multiple bipolar P - E loops were collected at intervals between E_{app} of 5 kV/cm to 20 kV/cm with samples being introduced to higher E_{app} on successive measurements between the minimum and maximum E_{app} .

3. Results and discussion

Laboratory X-ray Diffraction (XRD) confirmed the ceramics to be single-phase and the patterns fully indexed on a tetragonal unit cell. The ceramic microstructure consisted of grains that typically ranged from \sim 50 μm to 100 μm in size, with some smaller grains of \sim 20 μm , Supporting Information Fig. SI1. This type of grain structure, ranging from \sim 70 μm to 100 μm has been reported for other undoped BaTiO₃ ceramics sintered at a temperature of

1350/1355 °C [16–18]. The SEM images also revealed a low density of pores (the black spots), $\sim 4 \mu\text{m}$ in size and typically at the triple points of the grains. The measured density of the ceramics was $\sim 5.99 \text{ g/cm}^3$, yielding an overall density of 99.3% compared to the theoretical density of undoped BaTiO_3 (6.03 g/cm^3 [19]). The SEM images and measured densities confirm the microstructures obtained from these ceramics to be consistent with those reported from other studies on undoped BaTiO_3 using similar processing temperature/time profiles and their suitability for P – E testing.

A typical FTB bipolar P – E loop using an electric field of 20 kV/cm calculated and set using Equation 5 is shown in Fig. 3a (black line) with values of P_{max} , P_r and E_c of $\sim 19.4 \mu\text{C/cm}^2$, $11.0 \mu\text{C/cm}^2$ and 1.5 kV/cm, respectively. The polarisation values compare well with the range of literature values reported for undoped BaTiO_3 sintered at 1350 °C ($\sim 16 \mu\text{C/cm}^2$ to $22 \mu\text{C/cm}^2$) and for those of BaTiO_3 ceramics with grain sizes from $\sim 68 \mu\text{m}$ to $92 \mu\text{m}$ [20,21]. The coercive fields also match well with reported ranges (~ 1.5 – 2.0 kV/cm) for similar ceramics sintered at 1350 °C.

The effects of changing the top contact to a partially covered micro-contact to form mTFB electrodes are shown for the P – E measurements in Fig. 3a. The apparent polarisation of the material (*i.e.* P_{max} and P_r) increases with increasing S/r ratio compared to the FTB values despite the electric field reaching the same maximum value of 20 kV/cm in all cases, Fig. 3b–3c. The largest S/r yields the highest P_{max} of $\sim 70 \mu\text{C/cm}^2$, Fig. 3b, which is ~ 3.5 that for the FTB electrode configuration ($P_{\text{max}} \sim 19.4 \mu\text{C/cm}^2$). Similar trends are observed for P_r shown in Fig. 3c. With increasing S/r , the P – E loops become distorted and broader, especially for $S/r = 1.96$, where it is asymmetric with E_c rising from ~ 1.5 kV/cm (FTFB) to > 7 kV/cm, also shown in Fig. 3c.

The distortion and broadening of the P – E loops are also observed in the current-field (I – E) measurements. For FTB, Fig. 3d, there is a clear, well-defined peak increasing to $\sim 900 \mu\text{A}$ at the coercive field. As the current is low compared to this peak current, this indicates domain switching is the dominant contributor in the P – E response compared to the contributions from the conductivity or permittivity- electric field dependencies [22]. This provides a justification that the data can be referred to as a P – E loop; however, the I – E profile becomes significantly modified as the S/r ratio increases. The peak height reduces to $\sim 5 \mu\text{A}$ for $S/r = 1.96$ and is less well defined and broader as shown in Fig. 3e. Such a decrease in peak height and broadening has been shown to occur if there is a rise in the sample temperature in doped BaTiO_3 ceramics [22]. In this case, the conductivity of the sample is becoming a dominant component in the signal and as such there is low justification for referring to this as a P – E loop and really should be reported as a D – E response. It should be noted, that there also exists an asymmetry in this peak which could be linked to the contact radius and field direction.

S/r has a strong influence on the energy storage density. This is shown both in Table 1 for W_{rec} and W_{loss} , with the efficiencies for the respective P - E loop measurement also shown in Fig. 3f. It is worth stressing that the FTB configuration for these BaTiO_3 ceramics always provides the highest efficiency ($\sim 46\%$) compared to the mTFB electrodes, Table 1. For FTB and $S/r < 1$, W_{rec} is reasonably consistent until a value of $S/r = 1.96$, however, it is W_{loss} that increases throughout this range by over 14 times. This increase can be attributed to the change in the P - E loop due to the increased conductivity contribution in the measurement. As such the loop becomes distorted and loses its defined switching behaviour that is observed at FTB or lower S/r ratios, Fig. 3a. This increase in W_{loss} from 0.062 J/cm^3 to 0.890 J/cm^3 over the S/r range dramatically decreases the measured efficiency from $\eta \sim 46.1\%$ to 7.5% .

Table 1. Recoverable energy (W_{rec}) and energy loss (W_{loss}) with associated efficiencies η for BaTiO_3 ceramics with various mTFB S/r electrode arrangements measured from bipolar measurements. Values for full top and bottom electroded samples (FTB) are included for comparison.

	W_{rec} (J/cm^3)	W_{loss} (J/cm^3)	Efficiency, η
FTB	0.0532	0.0622	46.1
0.17	0.0502	0.125	28.7
0.25	0.0503	0.127	28.4
0.47	0.0548	0.161	25.3
0.77	0.0556	0.259	17.7
0.81	0.0456	0.393	10.4
0.97	0.0476	0.466	9.26
1.23	0.0579	0.563	9.32
1.96	0.0720	0.890	7.49

3.1 Design and analysis of computational model

To determine if the effects observed can be linked to the spreading of the electric current associated with the micro-contact, finite element (FE) modelling using COMSOL multi-physics was employed to simulate the experimental analysis procedure [23]. A computational model was constructed as a rectangle of width 3.85 mm, with a thickness set using Table S11. This was then axially revolved around its edge to create a disc of diameter 7.7 mm. Electrical boundary conditions were set along the lower surface to create a ground contact. The full or micro contact was then assigned to the top of the disc with a triangular (1 Hz) voltage applied, mimicking the experimental setup. The maximum V_{app} was scaled using the sample thickness (Equation 5) as shown in Fig. 4a to generate $E_{\text{app}} = 20 \text{ kV/cm}$ through the sample. All other boundaries were set to be electrically insulating. The thicknesses of $S = 0.33 \text{ mm}$ used in the case of $S/r = 0.17$ required $V_{\text{app}} = 660 \text{ V}$ to generate the desired $E_{\text{app}} = 20 \text{ kV/cm}$, whereas for $S/r = 0.81$ with a thickness of $S = 1.01 \text{ mm}$ a higher $V_{\text{app}} = 2020 \text{ V}$ was required to generate the equivalent E_{app} , Fig. 4a.

The Jiles-Atherton model [24–26] was used to simulate the ferroelectric behaviour of undoped BaTiO₃ (see SI for more details). This model allows the simulation of a ferroelectric material by assuming the total polarisation can be represented as a sum of reversible and irreversible parts. The properties required to describe the ferroelectric behaviour are saturation polarisation, domain wall density, inter-domain coupling, polarisation reversibility and pinning loss. These values were fitted by implementing an iterative regression analysis-based approach (least squares fitting) on the FTB experimentally determined data set. The resulting model parameters are shown in the Supplementary information, Table SI2. The simulation of the FTB model in Fig. 4b in red, compares well against the experimental data shown in black. Note that the analytical model developed here is not set up to exactly match the experimental data but to provide a controlled simulated P-E loop that can be subjected to changes in the S/r ratio and the associated changes or trends recorded and observed. The fitted parameters are maintained through all simulations presented here to provide a demonstration of how the material should respond with changes only in the S/r ratio and not through any additional losses, such as heating effects, which may occur experimentally.

Simulations were then performed for the range of S/r given in Table SI1 and plots of the polarisation experienced at the micro-contact versus the electric field were calculated from Equation 5 and are shown in Fig. 4c. Slim loops were obtained from the simulations with P_{\max} increasing from $\sim 21 \mu\text{C}/\text{cm}^2$ to $28 \mu\text{C}/\text{cm}^2$ but E_c decreasing from 2.25 kV/cm to 0.63 kV/cm as S/r increases from 0.17 to 1.96, respectively. A comparison of the experimental data versus the simulated data for the FTB and various S/r values is given in Fig. SI2. It is clear there is good agreement for FTB and $S/r = 0.17$, Fig. SI2a–2b, respectively but significant deviations occur for the larger S/r values of 0.97 and 1.96, Fig. SI2c–2d, respectively.

A cross-sectional view of the electric field at maximum V_{app} experienced by the material for various S/r ratios is shown in Fig. 4d and the electric field profile over the sample surface is highlighted in Fig. 4e and through the depth of the sample in Fig. 4f. The black line in Fig. 4d shows the length of the top micro contact in each case and for all three figures, the electric field is plotted on a log scale to show the large changes obtained.

For $S/r = 0.17$, the electric field generated for the majority of the contact surface area is 10 kV/cm, half of the assumed 20 kV/cm. Although this does rise to over 150 kV/cm at the edges of the contact, the integrated average electric field over the contact is 17 kV/cm, still below the value assumed in Fig. 4d–4e. On increasing S/r to 0.97 the field under the contact increases to 27 kV/cm due to the smaller size of the contact and it steadily rises to over 560 kV/cm at the edges, Fig. 4d–4e. This leads to an integrated average of 92 kV/cm over the entire contact surface. As S/r is further increased, the contact average dramatically rises to 229 kV/cm for $S/r = 1.96$, a factor of 11 higher than the assumed field. This can be attributed to the small size of the contact where the high concentration of field at the edges now

increases the electric field experienced at the centre and edges of the contact to 99 kV/cm and 650 kV/cm, respectively as shown in Fig. 4d–4e.

In all these cases, electrical confinement is not significant as the electric field at the external surface is as low as 1 V/cm, Fig. 4d. For low S/r ratios; however, there is visible electrode-to-electrode interference. For example, for $S/r = 0.17$, the high field envelope encompasses the lower electrode, shown by the flat response in Fig. 4f and this causes the resistance to decrease. As the contact is relatively wide, the edge effects from the contact do not interfere with the field at the centre and the field is uniform and extends across the contact surface relatively unchanged, Fig. 4e. As the thickness of the sample increases the high field envelope rises above the lower contact ($S/r = 0.97$) and moves to a lower interference configuration as shown by the drop in electric field in Fig. 4f. This creates greater current spreading and a higher, more localised, non-linear electric field to be present directly under the contact.

Extracting W_{rec} and W_{loss} from the simulated data in Fig. 4 highlights that the efficiency increases with S/r from 34.7% when simulating an FTB arrangement to 42.8% for $S/r = 1.23$. This increase, in contrast to the decrease observed experimentally, can be attributed to the large fields and more localised current under the contact which causes a greater proportion of saturated material in the measurement. These differences arise due to our simulations maintaining the fitted Jiles-Atherton model from the FTB data and assuming that the intrinsic material properties remain unchanged throughout the measurements, which is unlikely to be true [22].

	W_{rec} (J/cm ³)	W_{loss} (J/cm ³)	Efficiency, η
FTB	0.0419	0.0788	34.7
0.17	0.0830	0.1450	36.4
0.77	0.1170	0.1880	38.3
0.97	0.1770	0.2720	39.4
1.23	0.1780	0.2380	42.8
1.96	0.1760	0.2400	42.3

Table 2. Recoverable energy (W_{rec}) and energy loss (W_{loss}) with associated efficiencies η for the simulated results as shown in Fig. 4.

3.2 Comparison of experimental results and computational model

These models demonstrate that the experimentally applied electric field calculated by Equation 5 is an underestimate of the actual field the material is experiencing under the top contact. To determine the strength of this field we can use these simulations to integrate the

electric field over the micro-contact. This is shown as a function of S/r in Fig. 5a. There is a strong, non-linear rise in the field strength with increasing S/r . These electric fields are now used as scaling factors for both simulation and experimental data. As an example, for $S/r = 1.96$ the integrated electric field is 229 kV/cm compared to the assumed applied value of 20 kV/cm, generating a scaling factor of 11.5. Employing these factors, the electric field in the modelled data can be rescaled as shown in Fig. 4c, where now the $P-E$ loops overlay with similar $E_c \sim 2.25$ kV/cm values, Fig. 5b–5c. This highlights, when rescaled, the FTB and low S/r ratios are now minor loops of the larger S/r ratios as would be expected.

These same factors can also be applied directly to the experimental data in Fig. 3a and rescaled plots are shown in Fig. 5d. As shown, similar to the rescaled modelling data in Fig. 5b the $P-E$ loops now start to nest, in Fig. 5d. While the simulated $P-E$ loops match well with FTB and low S/r ratios, as S/r increases, significant deviations in the loop shape are observed (see SI and Fig. SI2) with the experimental data starting to clearly resemble the ‘cigar-shaped’ loops referred to in [2] due to the presence of additional losses. We note that although W_{rec} and W_{loss} alter due to the rescaling, as shown in Table 3, η remains the same as that shown in Table 1 and Fig. 3d due to the scaling cancelling in the efficiency calculation.

Table 3. Rescaled recoverable energy (W_{rec}) and energy loss (W_{loss}) of the $P-E$ loops with associated efficiency, η as a function of the S/r ratio.

S/r	Scale factor	W_{rec} (J/cm ³)	W_{loss} (J/cm ³)	Efficiency, η
FTB	1.000	0.0532	0.0622	46.10
0.17	0.870	0.0437	0.1090	28.70
0.25	1.030	0.0518	0.1310	28.40
0.47	2.070	0.1140	0.3340	25.30
0.77	2.600	0.1450	0.6720	17.70
0.81	3.610	0.1640	1.4200	10.40
0.97	4.630	0.2200	2.1600	9.26
1.23	5.940	0.3440	3.3400	9.32
1.96	11.500	0.8250	10.2000	7.49

For low S/r ratios, the $P-E$ loops follow a very similar profile, maintaining a slimmer shape and relatively high efficiency is obtained. As the S/r ratio rises above unity, the $P-E$ loops become broader, indicating greater energy loss, Fig. 5d and Table 3. As before for $S/r = 1.96$, the $P-E$ loop is distorted with a large enclosed area and a significant increase in W_{loss} to over 10 J/cm³, Table 3. The rescaled values for the electric field at this S/r ratio are extremely high, rising to over 200 kV/cm. The coercivity values obtained from the rescaled bipolar $P-E$ data in Fig. 5d versus S/r are shown in Fig. 5e. For S/r below ~ 0.5 , the slim $P-E$ loops with a well-defined saturated shape have a coercivity of < 4 kV/cm but it then rises steeply to > 80 kV/cm as the $P-E$ loops lose their saturated shape and become larger with greater loss. At

low S/r the loops again nest well. As the S/r ratio increases towards 1, the loops again become broader, indicating higher loss and lower efficiency, as shown in Table 3.

3.3 Discussion

The experimental and simulated $P-E$ results presented here show how relatively small changes in the electrode size and/or thickness of a sample can result in significant variability in the extracted material values for W_{rec} and especially W_{loss} via $P-E$ loop measurements. This discrepancy is driven by the variability of the electric field the material experiences under the partial contact, which is induced by changes in the S/r ratio. For low S/r ratios, the electric fields are typically uniform and match those estimated by Equation 5. This is also observed in the sharper peaks in the $I-E$ plots indicating domain switching dominating the response with little contribution from conductivity and the dielectric displacement. At higher S/r ratios, electric fields exceeding 600 kV/cm can be generated near the edge of the contacts, whereas they are below 100 kV/cm in the centre of the contact. This local electric field generates variations in the integrated current inducing additional contributions in the signal. As such, the $P-E$ loops become distorted, and the loss increases as the domain switching current is increasingly swamped in a signal that contains other contributions. It is clear from this, that the size of the contact and thickness of the sample play significant roles. For example, in our experiments, samples with $S/r = 0.47$ and 1.23 only differ in thickness by 0.04 mm (0.94 mm vs. 0.98 mm) but due to the contact size reducing from 2.0 mm to 0.5 mm, the efficiency of the material was more than halved decreasing from $\sim 25.3\%$ to 9.3%.

Although many research groups create contacts of the same size on their samples (*e.g.* via masks for microcontacts), the thickness of the samples (and therefore S/r) may vary and this can play a significant role. In particular, the thickness is used to calibrate the applied voltage using Equation 2 and our results show that it plays a key role in how the current spreads out from the micro-contact, and as such, the electric field distribution. For example, in the experimentally measured cases of $S/r = 0.77$ and 1.96, both possess the same micro-contact radius but their thickness differs by 0.59 mm (0.39 mm to 0.98 mm, respectively). This thicker sample causes the electric field to be strongly localised under the contact, broadening the loop and substantially increasing the loss. This results in the efficiency of the sample decreasing from $\sim 17.7\%$ to 7.5%.

As shown by Figure 5 and the efficiencies generated from the corrected data, there are still other phenomena reducing reliability. At low S/r ratios, the $P-E$ loops overlay and only small changes in efficiency are measured. As S/r increases, the electric field localises and a broadening in the $P-E$ loop is observed experimentally with associated changes in the $I-E$ plots. This distorted loop shape, which resembles the 'cigar-shaped' loops referred to in [2] is not seen through the modelled data and as such is arising from other factors associated with high fields, such as defect movement, irreversible domain movement, leakage in the

form of conductivity and/or joule heating. As noted in [2], there can be significant contributions to switched charge as highlighted in Equation 3. The asymmetry observed in the $I-E$ plots also indicates the frequency and direction of the field sweep could play a significant role in the loop shape. All these additional contributions illustrate that what is being measured is actually a $D-E$ loop which should not be assumed to represent the $P-E$ response of the sample. This can only be achieved with appropriate subtractions of the dielectric displacement and conductivity effects which can be challenging to determine. As such, only by using low S/r ratios with the largest contact size that can be created without leading to arcing would provide the greatest confidence in such measurements and in the assumption that it represents a $P-E$ loop response.

The results presented here are for ferroelectric BaTiO₃ ceramics where W_{rec} and η increase and decrease, respectively with increasing S/r . This is in contrast to a related study on NaNbO₃-based Anti-Ferro-Electric (AFE) materials where efficiency was reported to increase for a mTFB compared to an FTB arrangement [12]. Furthermore, mechanical self-confinement associated with radial compressive stresses exerted on the micro-top electroded area by the unelectroded portion of AFE Pb(Zr,Ti)O₃-based capacitors has been attributed to enhancing energy storage density [26]. This highlights that various trends with S/r may be observed depending on the type of non-linear dielectric material being investigated.

4. Conclusions

Since the 2008 article ‘ferroelectrics go bananas’ [2], the estimated number of peer-reviewed research articles referring to “polarization-electric field loops” has increased from ~300 to over 1400 in 2023, using a simple Google Scholar search. This technique now underpins and helps drive materials discovery/optimisation, especially in the development of efficient high-energy-density ceramic capacitors. Most of the published work indicates how changes in composition or processing affect the material’s energy density storage and performance, leading to new avenues of research. In these, however, few refer to their sample geometries and typically, only the applied voltage and assumed electric field based on Equation 2 is reported. In [2] Scott noted that many articles are “reporting completely meaningless coercive field and remanent polarization values extracted from cigar-shaped loops that are typical of lossy dielectrics and have very little to do with the true ferroelectric properties of the material studied”. Our work goes further to show that even if saturation is achieved, sample thickness (S) or electrode contact size (r) needs to be discussed to allow correct interpretation and meaningful comparisons to be made.

Here we have used ferroelectric BaTiO₃ as a non-linear dielectric and demonstrate the losses and extracted efficiencies from $P-E$ loop measurements to increase and decrease, respectively with increasing S/r . In the literature, however, there are reports of increasing

efficiencies based on partial as opposed to full electrode contacts on AFE NaNbO_3 - and $\text{Pb}(\text{Zr,Ti})\text{O}_3$ -based materials [12],[26]. It is therefore important that the research community that uses P - E type-measurements to report energy storage performance on the wide range of non-linear dielectrics, from ferroelectric, relaxor ferroelectric and AFE materials to consider if they are measuring P or D . The former is associated with ferroelectric domain switching, P ; however, the latter contains additional contributions from the dielectric displacement and electrical conductivity, σ of the material. In all cases, however, reporting the contact size and thickness of the samples used for measurements should be made allowing researchers to make better comparisons and gain more confidence and an informed understanding of the observed trends.

Declaration of competing interest

The authors declare they have no known competing financial interests or personal relationships that could have appeared to influence the work reported in this paper.

Acknowledgements

The authors would like to acknowledge the EPSRC funding to support this work through a CASE conversion DTP grant EP/T517835/1.

References

1. M E Lines and A M Glass, *Principles and applications of ferroelectrics and related materials*, Oxford University Press, 1977.
2. J F Scott, Ferroelectrics go bananas, *J Phys: Condens Matter* **20** (2008) 021001.
3. O Hideki, C A Randall and S Trolier-Mckinstry, High-energy density capacitors utilizing 0.7 BaTiO_3 -0.3 BiScO_3 , *J Am Ceram Soc* **92** [8] (2009) 1719–24.
4. H Qi, R Zuo, A Xie, A Tian, J Fu, Y Zhang, et al, Ultrahigh Energy-Storage Density in NaNbO_3 -Based Lead-Free Relaxor Antiferroelectric Ceramics with Nanoscale Domains, *Adv Func Mater* **29** [35] (2019) 1903877.
5. H Pan, F Li, Q Zhang, S Lan, Y Zheng, J Ma, et al, Ultrahigh-energy density lead-free dielectric films via polymorphic nanodomain design, *Science* **356** (2019) 578–82.
6. G Wang, Z Lu, Y Li, L Li, H Ji, A Feteira, et al, Electroceramics for high-energy density capacitors: Current status and future perspectives, *Chem Rev* **121** [10] (2021) 6124–72.
7. H Qi, A Xie, A Tian and R Zuo, Superior energy-storage capacitors with simultaneously giant energy density and efficiency using nanodomain engineered BiFeO_3 - BaTiO_3 - NaNbO_3 lead-free bulk ferroelectrics, *Adv Energy Mater* **10** (2020) 1903338.
8. G Wang, J Li, X Zhang, Z Fan, F Yang, A Feteira, et al. Ultrahigh energy storage density lead-free multilayers by controlled electrical homogeneity, *Energy Environ Sci* **12** (2019) 582–8.
9. H Qi and R Zuo, Linear-like lead-free relaxor antiferroelectric $(\text{Bi}_{0.5}\text{Na}_{0.5})\text{TiO}_3$ - NaNbO_3 with giant energy-storage density/efficiency and super stability against temperature and frequency, *J Mater Chem A* **7** (2019) 3971–8.
10. X Wang, Y Fan, B Zhang, A Mostaed, L Li, A Feteira, et al, High discharge energy density in novel $\text{K}_{1/2}\text{Bi}_{1/2}\text{TiO}_3$ - BiFeO_3 based relaxor ferroelectrics, *J Eu Ceram Soc* **42** [15] (2022) 7381–7.

11. K Prume, T Schmitz and S Tiedke, *Polar oxides: Properties, characterization, and imaging*; R Waser, U Böttger and S Tiedke, J Wiley & Sons, 2004.
12. M-H. Zhang, L Fulanovic, C Zhao and J Koruza, Review on field-induced phase transitions in lead-free NaNbO_3 -based antiferroelectric oxides for energy storage, *J Materiomics*, **9** [1] (2023) 1–18.
13. J Fleig and J Maier, Local conductivity measurements on AgCl surfaces using microelectrodes, *Solid State Ionics*, **85** (1996) 9–15.
14. R A Veazey, A S Gandy, D C Sinclair and J S Dean, Modeling the influence of two terminal electrode contact geometry and sample dimensions in electro-materials, *J Am Ceram Soc* **102** [6] (2019) 3609–22.
15. H Ma, D C Sinclair and J S Dean, A finite element study on the influence of surface cracks on micro-contact impedance spectroscopy measurements, *Solid State Ionics* **393** (2023) 116173
16. S Lee, U Paik, V A Hackley, Y-G Jung, and K-J Yoon, Microstructure and permittivity of sintered BaTiO_3 : Influence of particle surface chemistry in an aqueous medium, *Mater Res Bull* **39** [1] (2004) 93–102.
17. T Kanata, T Yoshikawa, and K Kubota, Grain-size effects on dielectric phase transition of BaTiO_3 ceramics, *Solid State Commun*, **62** [11] (1987) 765–7.
18. H-Y Lee, J-S Kim, N-M Hwang and D-Y Kim, Effect of sintering temperature on the secondary abnormal grain growth of BaTiO_3 , *J Eu Ceram Soc* **20** (2000) 731–7.
19. K Tsuji, A Ndayishimiye, S Lowum, R Floyd, K Wang, M Wetherington, et al, Single step densification of high permittivity BaTiO_3 ceramics at 300 °C, *J Eur Ceram Soc* **40** [4] (2020) 1280–4.
20. Y Huang, C Zhao, B Wu, and X Zhang, Grain size effects and structure origin in high performance BaTiO_3 -based piezoceramics with large grains, *J Eur Ceram Soc* **42** [6] (2022) 2764–71.
21. I Fujii and S Trolrier-McKinstry, Temperature dependence of dielectric nonlinearity of BaTiO_3 ceramics, *Microstructures* **3** (2023) 2023045.
22. H Yan, F Inam, G Viola, H Ning, H Zhang, Q Jiang, et al, The contribution of electrical conductivity, dielectric permittivity and domain switching in ferroelectric hysteresis loops, *J Adv Dielec* **1** [1] (2011) 107–18.
23. COMSOL Multiphysics® v. 6.1. www.comsol.com. COMSOL AB, Stockholm, Sweden.
24. D C Jiles and D L Atherton, Theory of ferromagnetic hysteresis, *J Appl Phys* **55** [6] (1984) 2115–20.
25. D C Jiles and D L Atherton, Theory of ferromagnetic hysteresis, *J Magn Magn Mater.* **61** (1986) 48–60.
26. D C Jiles, J B Thoelke and M K Devine, Numerical determination of hysteresis parameters for the modeling of magnetic properties using the theory of ferromagnetic hysteresis, *IEEE Trans Magn* **28** (1992) 27–35.
27. S E Young, J Y Zhang, W Hong and X Tan. Mechanical self-confinement to enhance energy storage density of antiferroelectric capacitors, *J Appl Phys* **113** [5] 20130054101.

Figure

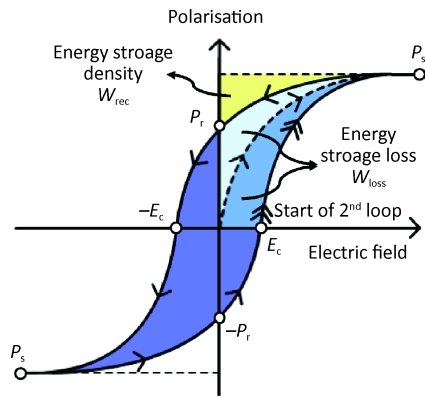
Fig. 1. A schematic representation of an 'ideal' P - E loop measurements highlighting the polarisation saturation (P_s), remanence (P_r) and coercive field E_c for a typical (non-conducting) ferroelectric material. Based on the upper right quadrant of the P - E loop, the yellow region shows the energy storage density W_{rec} , the light blue region shows the energy storage loss, W_{loss} for unipolar measurements, and the sum of the light and medium blue regions show W_{loss} for bipolar measurements. Arrows indicate measurement direction, with double arrows showing the start of the second loop.

Fig. 2. Schematic representations of current flow and electric field effects in various electrode contact measurements of a system with thickness S . (a) Full top-bottom (FTB) contacts where the current flows between the electrodes in a uniform manner. (b) A micro-contact of radius r with a full bottom contact, mTFB. Here the current and field spread outwards from the micro contact. The size of the contact compared to the dimensions of the sample can give rise to various scenarios (c–f) where the current and field can be confined and cause interference between the electrodes. The blue regions under the electrodes are of high current density or electric field.

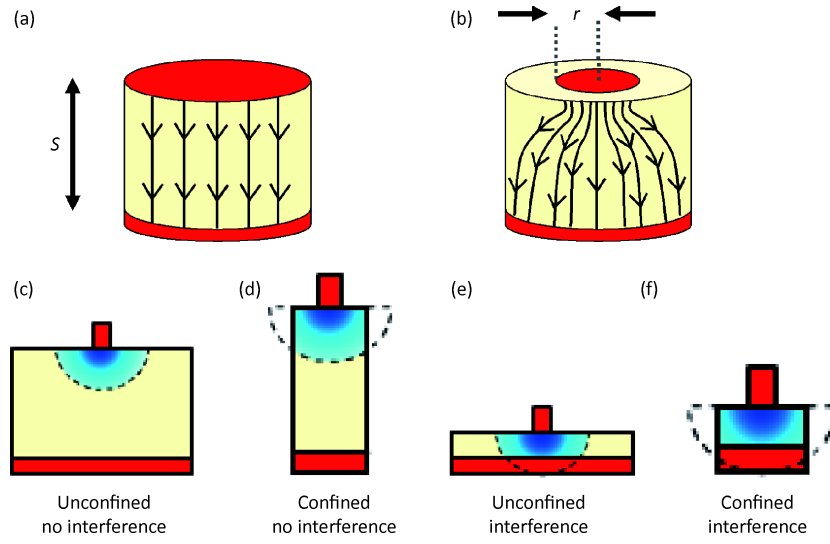
Fig. 3. (a) Experimental P – E loops of BaTiO₃ ceramics for various S/r ratios using the bipolar measurements. (b) the associated P_{\max} . (c) P_r (open symbols, left axis) and E_c (full red symbols, right axis) versus S/r . A guide to the eye is overlaid in both (b) and (c) to show the trend for P_{\max} and P_r , respectively. (d) I – E plots for a FTB system and (e) for the full S/r data set. (f) The calculated efficiency, η , versus S/r . The FTB contact configuration is overlaid as a comparison using an orange line.

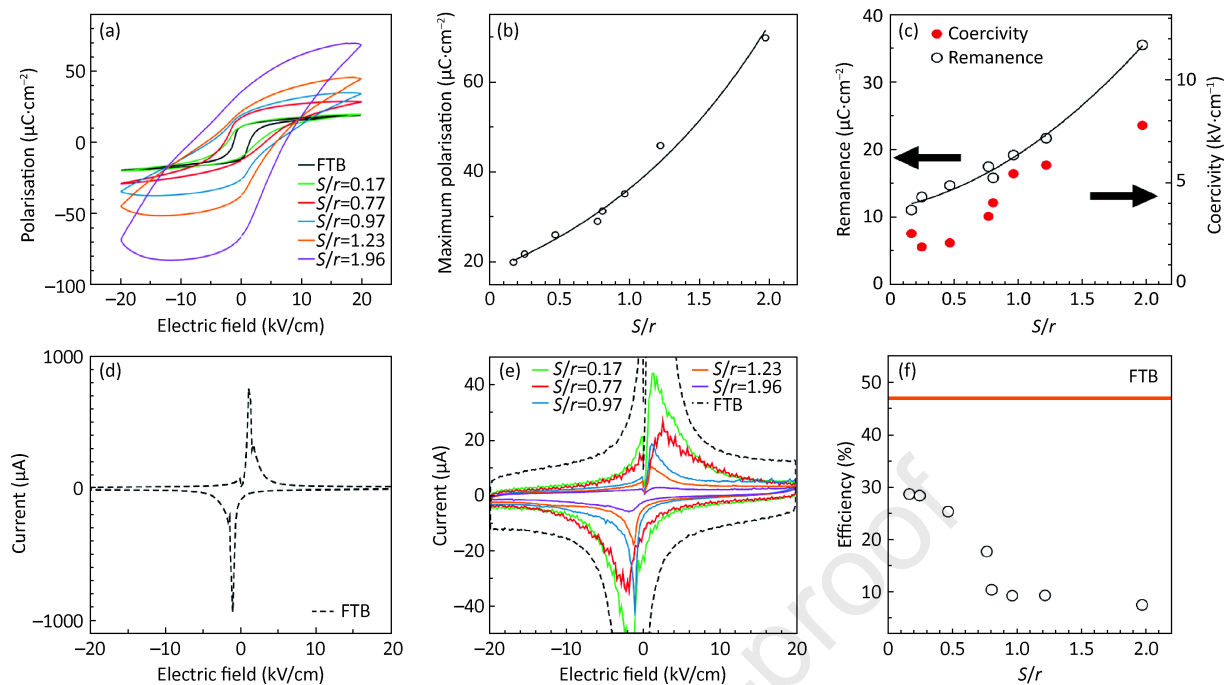
Fig. 4. Simulation of P – E loops using finite element modelling. (a) To be consistent with experiments the applied voltage, V_{app} , is scaled to thickness as shown for $S/r = 0.17$ and 0.81 . (b) An FTB experimentally determined P – E loop compared directly to the FE model using the Jiles-Atherton method [22–24]. (c) Simulated P – E loops for various S/r plotted versus the assumed electric field. (d) Cross-sections of the localised electric field experienced in the material for three S/r values where (e) shows the local electric field generated from the centre of the contact across the surface of the sample and (f) shows the electric field along the depth of the sample at the centre of the contact.

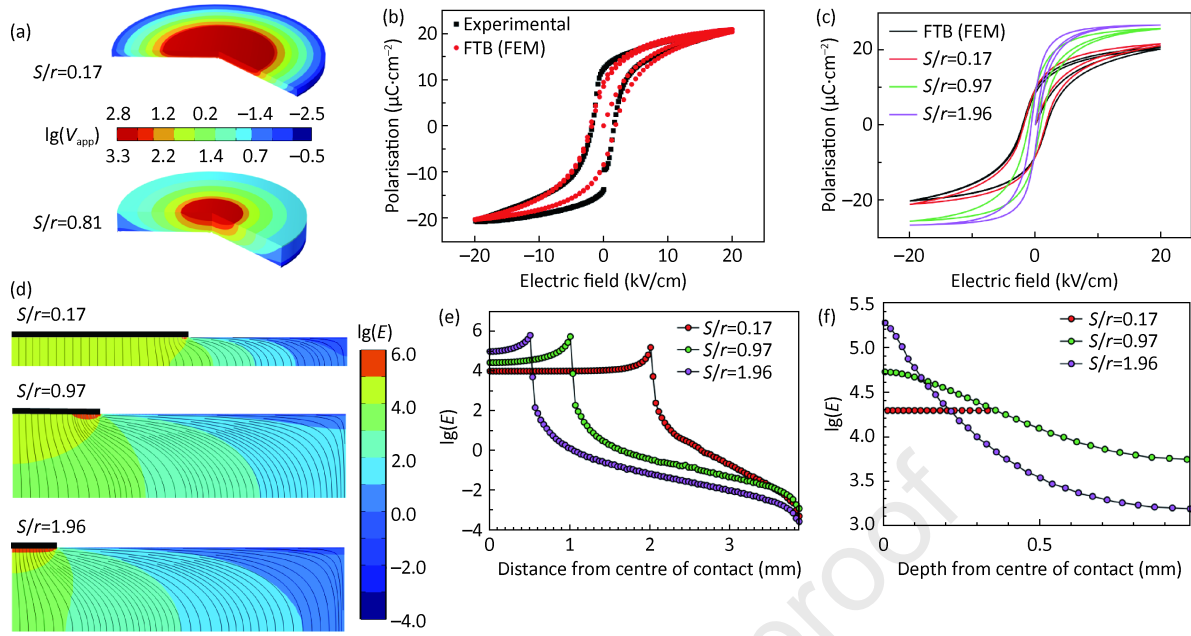
Fig. 5. (a) Integrated electric field on the micro-contacts for a range of S/r ratios. (b) Rescaled P – E loops of the modelled data shown in Fig. 4c with FTB and lower S/r ratios shown in (c) for clarity. (d) Experimental data from Fig. 3a replotted using the integrated fields. At low S/r the P – E loops nest but with increasing S/r increasing distortion of the loops becomes more evident. (e) Coercivity after rescaling the measurements versus S/r .

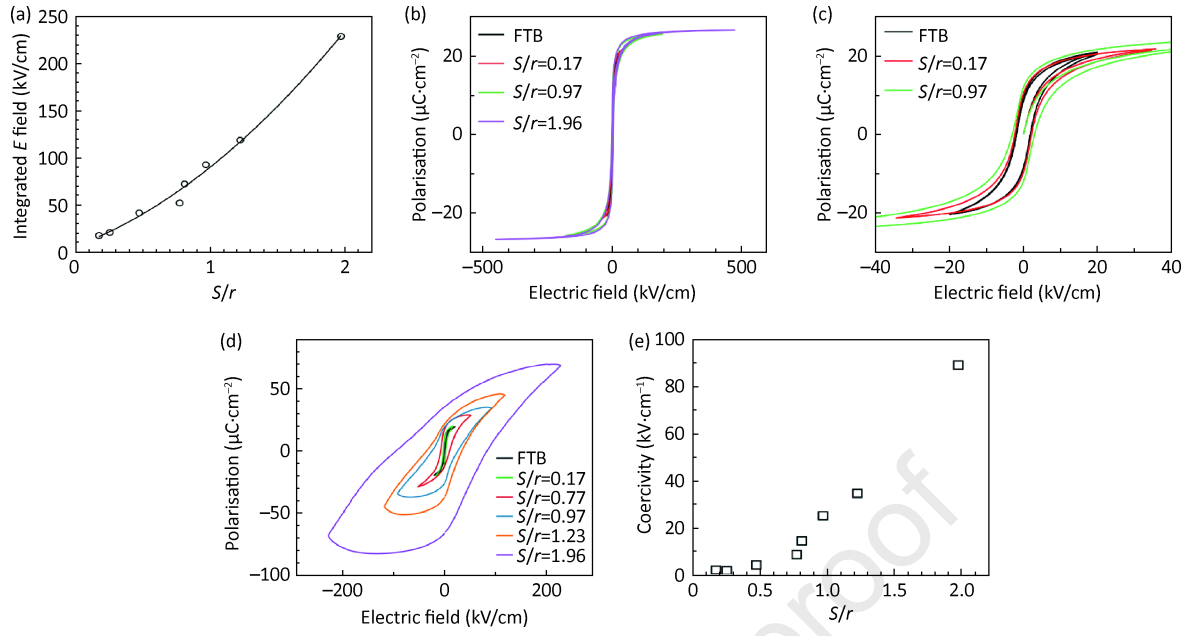


Journal Pre-proof









Highlights

- Experiments and finite element modelling (FE) explore bi-polar Polarisation-Electric field measurements in BaTiO₃ ceramics.
- The recoverable energy storage, loss and efficiency depend on the ratio of sample thickness (S) and top contact radius (r).
- A simple geometric correction for S underestimates the field experienced under the top contact at high S/r values.
- S and r are important parameters to report when using P - E loops to assess efficiency in non-linear dielectric materials.

The authors declare they have no known competing financial interests or personal relationships that could have appeared to influence the work reported in this paper.

Journal Pre-proof

Biography



Miss Erin Carroll received her MEng in Material Science and Engineering (research) in 2023 (Sheffield). She is studying her Ph.D. (Faculty award scholarship) on local structure-property relationships in A-site deficient perovskites supervised by Prof. Sinclair, Dr. Dean and Dr. Owen within the Functional Materials Group in the Department of Materials Science and Engineering at the University of Sheffield, UK.



Mr James Killeen received his MEng in Aerospace Engineering in 2020 (Sheffield) and is studying for his Ph.D. on next generation materials for Multi-Layer Ceramic Capacitors which is sponsored by KAVX Ltd and is supervised by Prof. Sinclair and Dr. Dean within the Functional Materials Group in the Department of Materials Science and Engineering at the University of Sheffield, UK.



Professor Antonio Feteira is a Professor in advanced functional oxides for electronic, energy and biomedical applications at Sheffield Hallam University, UK His research focuses on the establishment of composition-structure-property relationships in new advanced functional oxides along with the fabrication of prototype devices via 3D integration of these materials.



Dr. Julian Dean is a Senior lecturer in Materials Modelling within the Functional Materials Group in the Department of Materials Science and Engineering at the University of Sheffield, UK. He is recognised for simulating the effects of microstructure and electrical behaviour on both functional oxides and magnetic materials.



Professor Derek Sinclair is a Professor of Materials Chemistry within the Functional Materials Group in the Department of Materials Science and Engineering at the University of Sheffield, UK. He is recognised for his ability to probe the structure (crystal and defect)-composition-microstructure-property relationships in a wide range of functional oxides, spanning from polar dielectrics via mixed conductors to solid electrolytes.